

Adaptive Finite Elements with Algebraic Stabilization for Convection-Dominated Transport

Naveed Ahmed, * Abhinav Jha[†]

Abstract

We present a numerical investigation of residual-based a posteriori error estimation for finite element discretizations of convection-diffusion equations stabilized by algebraic flux correction and related algebraic stabilization techniques. In particular, we consider AFC schemes employing the BJK and Monolithic Convex (MC) limiters and algebraically stabilized methods including MUAS, SMUAS, and the BBK approach. The performance of the estimators and limiters are studied on adaptively refined meshes for several two-dimensional test problems, including boundary layers, interior layers, and a non-linear convection problem with solution-dependent transport.

The experiments assess accuracy, preservation of the discrete maximum principle, adaptive mesh behaviour, and computational efficiency. The results show that the interaction between stabilization and a posteriori error estimation depends strongly on mesh alignment and on the character of the convection field. In particular, for problems with moving or curved layers, the behaviour of the limiters differs significantly: strongly upwind-biased limiters provide the most accurate solutions, while smoother algebraic stabilizations lead to more efficient nonlinear iterations. The study also indicates that residual-based estimators remain reliable for both linear and nonlinear problems but may react to changes in limiter activation during adaptive refinement.

Overall, the numerical results clarify the practical behaviour of several widely used stabilization techniques within an adaptive framework and highlight aspects that are not yet fully explained by the current theory, particularly for nonlinear transport problems.

Keywords: steady-state convection-diffusion-reaction equations; algebraically stabilized finite element methods; a posteriori estimator; adaptive grid refinement

1 Introduction

This paper is devoted to the study of convection-diffusion-reaction (CDR) equations, which arise in a wide range of applications including, transport phenomena and species concentration models. The governing partial differential equation is given by

$$\begin{aligned} -\varepsilon \Delta u + \mathbf{b} \cdot \nabla u + cu &= f && \text{in } \Omega, \\ u &= u_D && \text{on } \Gamma_D, \\ \varepsilon \nabla u \cdot \mathbf{n} &= u_N && \text{on } \Gamma_N. \end{aligned} \tag{1}$$

Here, $\varepsilon > 0$ is the diffusion coefficient, \mathbf{b} is the convection (or advective) field, c is the reaction coefficient, and f is a source or sink term. The functions u_D and u_N specify the Dirichlet and Neumann boundary conditions, respectively. The equation is posed on a polygonal domain $\Omega \subset \mathbb{R}^d$ with $d \geq 2$, whose boundary Γ is partitioned into disjoint Dirichlet and Neumann components: $\Gamma = \Gamma_D \cup \Gamma_N$, with $\Gamma_D \cap \Gamma_N = \emptyset$.

*Center for Applied Mathematics and Bioinformatics Department of Mathematics and Natural Sciences, Gulf University for Science and Technology, Mubarak Al-Abdullah Area/West Mishref, Kuwait, ahmed.n@gust.edu.kw

[†]Department of Mathematics, Indian Institute of Technology Gandhinagar, Palaj, Gandhinagar, 382055, Gujarat, India abhinav.jha@iitgn.ac.in

In the convection-dominated regime, where $L\|\mathbf{b}\|_{\infty,\Omega} \gg \varepsilon$ and L is the characteristic length scale (e.g., the domain diameter), the solution of Eq. (1) typically develops sharp gradients in narrow regions of the domain—known as interior and boundary layers. Moreover, solutions to Eq. (1) are known to satisfy maximum principles. This motivates the development of numerical methods that not only capture these layers accurately but also preserve a discrete analog of the maximum principle, known as the Discrete Maximum Principle (DMP). Standard discretization techniques, such as the finite difference or finite element methods, often fail in both respects: they may introduce spurious under- and overshoots due to violation of the DMP, and they may inadequately resolve sharp layers. As a result, the numerical solutions may be physically unreliable and unsuitable for practical use, see [41].

Keeping these two properties in mind, stabilization techniques were developed. One of the most prominent stabilization schemes is the Streamline Upwind Petrov Galerkin (SUPG) scheme developed by Brooks and Hughes [12]. They approximate these layers well but fail to satisfy the DMP; hence, under and overshoots can be observed in the vicinity of layers. Other linear schemes, such as Upwind[20], Local Projection Stabilization (LPS) [33], Spurious Oscillations at Layers Diminishing (SOLD) [29] have the same issues. We refer to [41] for an overview of these methods. Nonlinear stabilization schemes are a small class of techniques that not only approximate these layers but also satisfy the DMP. The idea of non-linear stabilization can be traced back to the work of Zalesak [46]. However, it has gained popularity through the work of Kuzmin and co-authors [36, 37, 39] and is referred to as *Algebraic Flux Correction* (AFC) schemes. The numerical analysis of these schemes has been developed in [6], and further improvements have been proposed in [7, 38, 35]. Recently, a more generalized approach has been presented in [30, 34] called *Algebraic Stabilizations*. Here the symmetric conditions of the limiters are dropped and an upwind type method is proposed. We refer to [8] for a detailed review of these methods.

Another way to resolve the layers is to use non-equidistant meshes. Generally, there are two approaches to using non-equidistant meshes: predetermined meshes, such as the Shishkin mesh [40], or adaptive meshes generated by a posteriori error estimators [4]. In this paper, we focus on a posteriori error estimators. Much work has been done to develop a posteriori error estimators for Eq. (1) and linear stabilization methods. One of the first numerical studies was done in [28], where it was shown that none of the estimators was robust to ε . By robustness, we mean that the constants appearing in the estimators should be independent of convection dominance. A robust estimator was developed in [43], where a dual-norm approach was used, and its generalization to linear stabilization schemes was developed in [42]. In [32], a robust estimator was also developed for the SUPG scheme, but in the natural norm of the system, that is, the SUPG norm, but here the analysis relied on certain assumptions. Lastly, a posteriori estimators in different norms, such as L^1, L^2 , and L^∞ can be found in [17, 18, 16, 14], respectively.

Very limited work exists at the intersection of a posteriori error estimation and AFC schemes. The first notable contribution in this direction was made in [2], where a fully computable, albeit non-robust, estimator was developed for linearity-preserving algebraic stabilization techniques. Subsequently, a residual-based non-robust estimator, independent of the choice of flux limiters, was proposed in [22] specifically for AFC schemes. This work also integrated the SUPG-based estimator from [32] within the AFC framework. Both studies focused on the energy norm of the underlying system.

Further developments were presented in [26], which extended the residual-based estimator to non-conforming meshes. Three algebraic stabilization schemes were examined: the AFC method with the Kuzmin limiter [36], the AFC method with the BJK limiter [7], and the Monotone Upwind-type Algebraically Stabilized (MUAS) method [30]. Since the residual estimator predates the MUAS formulation, the stabilization contribution in MUAS was omitted in the analysis. More recently, [23] extended the analysis from [22] to a more general algebraic stabilization framework that includes the MUAS method and its improved variant, the Symmetric Monotone Upwind-type Algebraically Stabilized (SMUAS) method, introduced in [34]. While [23] primarily focused on theoretical analysis and included only basic numerical experiments, it demonstrated promising performance for SMUAS in preliminary studies. However, that study did not include another algebraic stabilized method which is based on the local smoothness indicator known as the BBK method [5], which are incorporated in the present work.

The present work builds on these foundations by offering a more comprehensive numerical evaluation of

a posteriori error estimators and various algebraic flux limiters. The main contributions of this study are as follows:

- A detailed numerical assessment in two dimensions of AFC and algebraic stabilization schemes for adaptively refined grids.
- Inclusion of numerical studies for the Monolithic Convex Limiting (MC) scheme [38], as well as the BBK method [5, 9], which were absent in prior analyses.
- Numerical experiments involving nonlinear problems. To the best of our knowledge, prior numerical studies on AFC schemes have been limited to linear examples; in this work, we present results for nonlinear cases as well.

It is worth noting that previous numerical assessments of these methods have largely been conducted on uniformly refined meshes; see [25, 24, 27, 31]. In contrast, the current work focuses on adaptively refined meshes, offering new insights into their performance in more practical computational settings.

The structure of the paper is as follows. In Section 2, we provide a unified overview of the algebraic stabilization schemes considered in this study. Section 3 presents an overview of the important theorems for the residual-based a posteriori error estimators. In Section 4, we carry out detailed numerical experiments, focusing on adaptive mesh refinement and a range of relevant parameters. Finally, Section 5 summarizes the main findings.

2 Algebraic Stabilization Schemes

Throughout this paper standard notions for Sobolev spaces and their norms are used, [1]. Let $\Omega \subset \mathbb{R}^d$, $d \geq 2$ be a measurable set, then the L^2 -inner product is defined by (\cdot, \cdot) and its duality pairing by $\langle \cdot, \cdot \rangle$. The norm (semi-norm) on $W^{m,p}(\Omega)$ is denoted by $\|\cdot\|_{m,p,\Omega}(|\cdot|_{m,p,\Omega})$ with the convention $W^{m,2}(\Omega) = H^m(\Omega)$ and $\|\cdot\|_{m,\Omega} = \|\cdot\|_{m,2,\Omega}$ (similarly $|\cdot|_{m,\Omega} = |\cdot|_{m,2,\Omega}$).

It is well-known that under the assumption

$$c(x) - \frac{1}{2} \nabla \cdot \mathbf{b}(x) \geq \sigma > 0, \quad (2)$$

Eq. (1) possess an unique weak solution $u \in \mathcal{C}(\overline{\Omega}) \cap H_D^1(\Omega)$ satisfying

$$a(u, v) = \langle f, v \rangle + \langle g, v \rangle_{\Gamma_N} \quad \forall v \in H_{0,D}^1(\Omega),$$

with

$$\begin{aligned} a(u, v) &= \varepsilon(\nabla u, \nabla v) + (\mathbf{b} \cdot \nabla u, v) + (cu, v), \\ H_D^1(\Omega) &= \{v \in H^1(\Omega) : v|_{\Gamma_D} = u_D\}, \\ H_{0,D}^1(\Omega) &= \{v \in H^1(\Omega) : v|_{\Gamma_D} = 0\}, \end{aligned}$$

and $\langle \cdot, \cdot \rangle_{\Gamma_N}$ is the duality pairing restricted to the Neumann boundary, e.g., see [41, Sec. III.1.1].

The algebraic stabilizations schemes for Eq. (1) reads as (see [30]): Find $u_h \in W_h$ ($\subset \mathcal{C}(\overline{\Omega}) \cap H_D^1(\Omega)$) such that

$$a_{AS}(u_h; u_h, v_h) = \langle f, v_h \rangle + \langle g, v_h \rangle_{\Gamma_N} \quad \forall v_h \in V_h, \quad (3)$$

with $a_{AS}(\cdot, \cdot, \cdot) : H_D^1(\Omega) \times H_D^1(\Omega) \times H_{0,D}^1(\Omega) \rightarrow \mathbb{R}$ such that

$$a_{AS}(u; v, w) = a(u, v) + b_h(u; v, w),$$

where W_h, V_h are linear finite-dimensional subspaces of $\mathcal{C}(\overline{\Omega}) \cap H_D^1(\Omega)$ and $\mathcal{C}(\overline{\Omega}) \cap H_{0,D}^1(\Omega)$, respectively and $b_h(\cdot, \cdot, \cdot)$ is the nonlinear stabilization term.

For AFC schemes such as those presented in [6, 7, 10], the stabilization term is defined as

$$b_h(u; v, w) = \sum_{i,j=1}^N (1 - \alpha_{ij}(u)) d_{ij} (v(x_j) - v(x_i)) w(x_i), \quad \forall u, v, w \in \mathcal{C}(\bar{\Omega}), \quad (4)$$

where $\mathbb{D} = \{d_{ij}\}$ is the artificial diffusion matrix, given by

$$d_{ij} = -\max \{a_{ij}, 0, a_{ji}\}, \quad i \neq j, \quad d_{ii} = -\sum_{i \neq j} d_{ij}. \quad (5)$$

Here, a_{ij} are the entries of the stiffness matrix associated with Eq. (1), N denotes the total number of nodes, and $\alpha_{ij}(u) \in [0, 1]$ are the *symmetric* solution-dependent flux limiters. In this work, we consider two types of limiters: the *BJK* limiter [7], and the *Monolithic Convex* (MC) limiter [38].

For the algebraic stabilization schemes proposed in [30, 34], the symmetry condition on the limiters is relaxed. The stabilization term is defined as

$$b(u; v, w) = \sum_{i,j=1}^N b_{ij}(u) v(x_j) w(x_i) \quad \forall u, v, w \in \mathcal{C}(\bar{\Omega}), \quad (6)$$

where

$$b_{ij}(u) = -\max \{(1 - \alpha_{ij}(u)) a_{ij}, 0, (1 - \alpha_{ji}(u)) a_{ji}\}, \quad i \neq j, \quad b_{ii}(u) = -\sum_{i \neq j} b_{ij}(u),$$

and $\alpha_{ij}(u) \in [0, 1]$ are non-symmetric flux limiters.

The BBK method presented in [5] can also be considered as an algebraic stabilized method with $b_{ij}(u)$ defined by

$$b_{ij}(u) = d_{ij} \gamma_{ij}(u), \quad i \neq j, \quad b_{ii}(u) = -\sum_{i \neq j} b_{ij}(u). \quad (7)$$

The concrete values of $\gamma_{ij}(u)$ would be given later.

We observe that in both Eq. (4) and Eq. (6), the stabilization term is linear in its second and third arguments.

In all the methods considered in this paper, the computation of limiters follows a two-step approach. First, the Galerkin finite element discretization is applied, incorporating Neumann boundary conditions. Once the limiters are computed, the Dirichlet boundary conditions are then imposed in the standard manner.

In the following, we describe the flux limiters and algebraic stabilization schemes that are studied in this work.

2.1 BJK Limiter

This method was proposed in [7], and it is shown that, for \mathbb{P}_1 elements, the method can be made linearity preserving.

The computation of the limiter starts with a pre-processing step by setting

$$a_{ji} := 0 \quad \text{if } a_{ij} < 0, \quad i = 1, \dots, M, \quad j = M + 1, \dots, N,$$

where M denote the number of non-Dirichlet degrees of freedom, compare [7, Eq. (2.4)]. For a real number a , denote $a^+ = \max\{a, 0\}$ and $a^- = \min\{a, 0\}$ then, the computation proceeds as follows:

1. Compute

$$P_i^+ = \sum_{j=1}^N (d_{ij}(u_j - u_i))^+, \quad P_i^- = \sum_{j=1}^N (d_{ij}(u_j - u_i))^-.$$

2. Compute

$$Q_i^+ = q_i (u_i - u_i^{\max}), \quad Q_i^- = q_i (u_i - u_i^{\min}),$$

with

$$u_i^{\max} = \max_{j \in N_i \cup \{i\}} u_j, \quad u_i^{\min} = \min_{j \in N_i \cup \{i\}} u_j, \quad q_i = \sum_{j \in N_i} \gamma_i d_{ij},$$

where

$$N_i = \{j \in \{1, \dots, N\} \setminus \{i\} : a_{ij} \neq 0 \text{ or } a_{ji} > 0\} \quad (8)$$

and γ_i is a positive constant. For \mathbb{P}_1 elements, a value of γ_i is used which guarantees the linearity preservation, see [7, Eq. 6.5] for details.

3. Compute

$$R_i^+ = \min \left\{ 1, \frac{Q_i^+}{P_i^+} \right\}, \quad R_i^- = \min \left\{ 1, \frac{Q_i^-}{P_i^-} \right\}, \quad i = 1, \dots, M.$$

If P_i^+ or P_i^- is zero, one sets $R_i^+ = 1$ or $R_i^- = 1$, respectively. The values for R_i^+ and R_i^- are set to 1 also for Dirichlet nodes.

4. Compute

$$\bar{\alpha}_{ij} = \begin{cases} R_i^+ & \text{if } d_{ij}(u_j - u_i) > 0, \\ 1 & \text{if } d_{ij}(u_j - u_i) = 0, \\ R_i^- & \text{if } d_{ij}(u_j - u_i) < 0, \end{cases} \quad i, j = 1, \dots, N.$$

5. Finally, one sets

$$\alpha_{ij} = \min \{ \bar{\alpha}_{ij}, \bar{\alpha}_{ji} \}, \quad i, j = 1, \dots, N.$$

In [7], it was shown that the method is DMP satisfying on arbitrary grids. In [24], it was observed that solving the nonlinear system of equations arising from the BJK limiter was harder than for other AFC methods.

2.2 Monolithic Convex Limiter

In [38], an algebraic stabilization technique was introduced for hyperbolic conservation laws. This method is demonstrated to yield a well-defined steady-state limit for the nonlinear discrete problem, irrespective of the chosen time step. Consequently, it presents a viable approach for discretizing steady-state equations. Although [38] does not incorporate diffusion effects, [27] employed the monolithic convex (MC) limiter to solve a steady-state convection-diffusion equation, yielding encouraging outcomes. The computation of these limiters is described by the following formula:

$$\alpha_{ij} = \begin{cases} \min \left\{ 1, \min \left\{ \frac{2d_{ij}(\bar{u}_{ij} - u_i^{\max})}{d_{ij}(u_j - u_i)}, \frac{2d_{ij}(u_j^{\min} - \bar{u}_{ji})}{d_{ij}(u_j - u_i)} \right\} \right\} & \text{if } d_{ij}(u_j - u_i) > 0, \\ 0 & \text{if } d_{ij}(u_j - u_i) = 0, \\ \min \left\{ 1, \min \left\{ \frac{2d_{ij}(\bar{u}_{ij} - u_i^{\min})}{d_{ij}(u_j - u_i)}, \frac{2d_{ij}(u_j^{\max} - \bar{u}_{ji})}{d_{ij}(u_j - u_i)} \right\} \right\} & \text{otherwise,} \end{cases} \quad (9)$$

where \bar{u}_{ij} are intermediate states defined by

$$2d_{ij}\bar{u}_{ij} = d_{ij}(u_i + u_j) + a_{ij}(u_j - u_i)$$

and

$$u_i^{\max} = \max_{j \in S_i} u_j, \quad u_i^{\min} = \min_{j \in S_i} u_j. \quad (10)$$

In the last formula, $S_i = \{j \in \{1, \dots, N\} : a_{ij} \neq 0\}$ that is the integer set containing the indices of node i and its nearest neighbors. Note that the definition of u_i^{\max} and u_i^{\min} can be changed to ensure linearity preservation [38, Section 6.1]. A local DMP for the algebraic system corresponding to the discretization of the steady-state (transport) problem was also proved in this paper. Numerical studies on uniformly refined grids were performed in [31] and it was observed that the efficiency of the MC limiter is better than the BJK limiter.

2.3 MUAS Method

Till now, we have considered symmetric limiters. For the algebraic stabilizations schemes proposed in [30], the symmetric condition is dropped on α_{ij} . This is an upwind type method referred to as Monotone Upwind-Type Algebraically Stabilized (MUAS) and the limiters are computed as follows:

1. Compute

$$P_i^+ = \sum_{j=1, a_{ij}>0}^N a_{ij}(u_i - u_j)^+, \quad P_i^- = \sum_{j=1, a_{ij}>0}^N a_{ij}(u_i - u_j)^-.$$

2. Compute

$$Q_i^+ = \sum_{j=1}^N \max \{|a_{ij}|, a_{ji}\} (u_j - u_i)^+, \quad Q_i^- = \sum_{j=1}^N \max \{|a_{ij}|, a_{ji}\} (u_j - u_i)^-.$$

3. Compute

$$R_i^+ = \min \left\{ 1, \frac{Q_i^+}{P_i^+} \right\}, \quad R_i^- = \min \left\{ 1, \frac{Q_i^-}{P_i^-} \right\}, \quad i = 1, \dots, M.$$

If P_i^+ or P_i^- is zero, one sets $R_i^+ = 1$ or $R_i^- = 1$, respectively. The values of R_i^+ and R_i^- are set to 1 for Dirichlet nodes as well.

4. Define

$$\alpha_{ij} = \begin{cases} R_i^+ & \text{if } u_i > u_j, \\ 1 & \text{if } u_i = u_j, \\ R_i^- & \text{if } u_i < u_j, \end{cases} \quad i, j = 1, \dots, N.$$

Local and global DMP have been shown in [30] to be valid on arbitrary simplicial meshes, but this method is not linearity preserving.

2.4 SMUAS Method

Recently, a further extension of the MUAS method has been proposed in [34] called the Symmetrized Monotone Upwind Type Algebraically Stabilized (SMUAS) method, which is an upwind type linearity-preserving limiter that satisfies DMP on arbitrary meshes. The limiters are computed as follows:

1. Compute

$$P_i^+ = \sum_{j \in S_i} |d_{ij}| \{(u_i - u_j)^+ + (u_i - u_{ij})^+\},$$

$$P_i^- = \sum_{j \in S_i} |d_{ij}| \{(u_i - u_j)^- + (u_i - u_{ij})^-\}.$$

2. Compute

$$Q_i^+ = \sum_{j \in S_i} \max\{|a_{ij}|, a_{ji}\} \{(u_j - u_i)^+ + (u_{ij} - u_i)^+\},$$

$$Q_i^- = \sum_{j \in S_i} \max\{|a_{ij}|, a_{ji}\} \{(u_j - u_i)^- + (u_{ij} - u_i)^-\}.$$

3. Compute

$$R_i^+ = \min \left\{ 1, \frac{Q_i^+}{P_i^+} \right\}, \quad R_i^- = \min \left\{ 1, \frac{Q_i^-}{P_i^-} \right\}, \quad i = 1, \dots, M.$$

If P_i^+ or P_i^- is zero, one sets $R_i^+ = 1$ or $R_i^- = 1$, respectively. The values of R_i^+ and R_i^- are set to 1 for Dirichlet nodes as well.

4. Define

$$\alpha_{ij} = \begin{cases} R_i^+ & \text{if } u_i > u_j, \\ 1 & \text{if } u_i = u_j, \\ R_i^- & \text{if } u_i < u_j, \end{cases} \quad i, j = 1, \dots, N.$$

In the above definition $u_{ij} = u_i + \nabla u_h|_{K_i^j} \cdot (x_i - x_j)$ for all $j \in S_i$. Here K_i^j is a mesh cell containing x_i that is intersected by the half line $\{x_i + \theta(x_i - x_j) : \theta > 0\}$. In [34], optimal convergence rates were observed numerically, whereas the Kuzmin, BJK, and the MUAS methods did not have the optimal rates.

Remark 1 For the computation of the SMUAS method, it is necessary to evaluate $\nabla u_h|_{K_i^j}$ at each nonlinear iteration. This step is computationally expensive. To mitigate this issue, at the beginning of the nonlinear loop, we store the cell number and the coordinates of the reflected point x_j , and subsequently use these stored values to compute the gradient and, in turn, u_{ij} .

Remark 2 In the SMUAS method, if i is a Neumann node, then the coefficient α_{ij} is computed using the MUAS method.

2.5 BBK Method

The last algebraic stabilization method we consider is the BBK method, originally presented in [5]. In Eq. (7), the factors $\gamma_{ij}(u)$ are computed as

$$\gamma_{ij}(u) = [\max\{\alpha_i(u), \alpha_j(u)\}]^p, \quad i, j = 1, 2, \dots, N,$$

where

$$\alpha_i(u) = \begin{cases} \frac{\left| \sum_{j \in S_i} (u_i - u_j) \right|}{\sum_{j \in S_i} |u_i - u_j|}, & \text{if } \sum_{j \in S_i} |u_i - u_j| \neq 0, \\ 0, & \text{otherwise,} \end{cases}$$

and for Dirichlet nodes we set $\alpha_i(u) = 0$ for $i = M + 1, \dots, N$. The exponent p controls the rate at which the artificial diffusion decays; following [9], we choose $p = 10$. A limited numerical study of the BBK method exists, and a comparison can be found in [31].

Remark 3 The BBK method used here is a modification of the original BBK method proposed in [5] and later reformulated in [9]. This reformulation is necessary because the original method cannot be written in the standard AFC framework: it may be the case that $b_{ij}(u) = 0$ even when $d_{ij} \neq 0$.

3 A Posteriori Error Estimators

This section reviews the a posteriori error estimators developed in [23].

Before presenting the results, we provide some details about the mesh triangulation. Let $\{\mathcal{T}_h\}_{h>0}$ denote a family of conforming triangulations of the domain Ω , where each triangulation \mathcal{T}_h consists of simplices and has characteristic mesh size

$$h := \max_{K \in \mathcal{T}_h} h_K.$$

We assume that each triangulation is admissible, meaning that any two elements are either disjoint or share a complete m -dimensional face for some $0 \leq m \leq d-1$. Furthermore, the mesh is assumed to be shape-regular.

The set of all edges is denoted by \mathcal{E}_h , and the set of edges associated with an individual element $K \in \mathcal{T}_h$ is denoted by $\mathcal{E}_h(K)$. The set of all faces is denoted by

$$\mathcal{F}_h = \mathcal{F}_{h,\Omega} \cup \mathcal{F}_{h,D} \cup \mathcal{F}_{h,N},$$

where $\mathcal{F}_{h,\Omega}$, $\mathcal{F}_{h,D}$, and $\mathcal{F}_{h,N}$ refer to the sets of interior, Dirichlet boundary, and Neumann boundary faces, respectively. In two dimensions, faces coincide with edges, and we have $\mathcal{F}_h = \mathcal{E}_h$.

Our analysis is carried out in the energy norm, which is given by

$$\|u\|_a^2 = \varepsilon \|\nabla u\|_{0,\Omega}^2 + \sigma \|u\|_{0,\Omega}^2.$$

Theorem 4 *Let $u_h \in W_h$ be a solution of Eq. (3). Then the global a posteriori error estimate in the energy norm is given by*

$$\|u - u_h\|_a^2 \leq \eta^2 := \eta_1^2 + \eta_2^2 + \eta_3^2, \quad (11)$$

where

$$\begin{aligned} \eta_1^2 &:= \sum_{K \in \mathcal{T}_h} \min \left\{ \frac{4C_I^2}{\sigma}, \frac{4C_I^2 h_K^2}{\varepsilon} \right\} \|R_K(u_h)\|_{0,K}^2, \\ \eta_2^2 &:= \sum_{F \in \mathcal{F}_h} \min \left\{ \frac{4C_F^2 h_F}{\varepsilon}, \frac{4C_F^2}{\sigma^{1/2} \varepsilon^{1/2}} \right\} \|R_F(u_h)\|_{0,F}^2, \\ \eta_3^2 &:= \sum_{E \in \mathcal{E}_h} \min \left\{ \frac{4\kappa_1 h_E^2}{\varepsilon}, \frac{4\kappa_2}{\sigma} \right\} |b_E|^2 h_E^{1-d} \|\nabla u_h \cdot \mathbf{t}_E\|_{0,E}^2, \end{aligned}$$

and the element and face residuals are defined as follows:

$$\begin{aligned} R_K(u_h) &:= f + \varepsilon \Delta u_h - \mathbf{b} \cdot \nabla u_h - c u_h \quad \text{in } K, \\ R_F(u_h) &:= \begin{cases} -\varepsilon [\![\nabla u_h \cdot \mathbf{n}_F]\!]_F & \text{if } F \in \mathcal{F}_{h,\Omega}, \\ u_N - \varepsilon (\nabla u_h \cdot \mathbf{n}_F) & \text{if } F \in \mathcal{F}_{h,N}, \\ 0 & \text{if } F \in \mathcal{F}_{h,D}, \end{cases} \end{aligned}$$

where $[\![\cdot]\!]$ denotes the jump across the face F , and \mathbf{n}_F is the outward-pointing unit normal to F .

Remark 5 *Several constants appear in Theorem 4, which we now describe. The constant C_I denotes the interpolation constant (see [11, Corollary 4.8.15]), and C_F arises from the face residual estimates (see [44, Lemma 3.1]). The constants κ_1 and κ_2 are defined as*

$$\kappa_1 = C C_{\text{edge,max}} \left(1 + (1 + C_I)^2 \right), \quad \kappa_2 = C C_{\text{inv}}^2 C_{\text{edge,max}} \left(1 + (1 + C_I)^2 \right),$$

where C is a generic constant independent of the mesh size h , C_{inv} is the inverse inequality constant (see [11, Lemma 4.5.3]), and $C_{\text{edge,max}}$ is a computable constant introduced in [22, Remark 9].

Remark 6 We would like to highlight a few remarks regarding the a posteriori error bound. First, we note that the estimator is not robust to the parameter ε , a well-known limitation of energy-norm estimates. An alternative is to employ duality-based techniques, as proposed in [42]; however, extending such approaches to nonlinear models presents significant challenges.

Next, we address the estimator's efficiency, specifically the local lower bound. A formal local lower bound for the estimator exists without requiring any assumptions on the stabilization term. It is termed formal because the local error is not directly bounded by the residual as is standard in the literature, but rather by a term that decays at the optimal rate.

4 Numerical Studies

This section presents the numerical assessment of the a posteriori error estimator introduced in Sec. 3. We compare different algebraic stabilization schemes from Sec. 2 on adaptively refined grids using a set of performance metrics.

The general strategy for solving an a posteriori error problem follows the loop:

$$\mathbf{SOLVE} \rightarrow \mathbf{ESTIMATE} \rightarrow \mathbf{MARK} \rightarrow \mathbf{REFINE}. \quad (12)$$

We now go over each step and provide relevant details.

- **SOLVE:** The solution procedure for the AFC scheme on uniform grids has been discussed in detail in [25, 24]. We provide a brief overview here. Let the system of equations corresponding to Eq. (3) be written as

$$(\mathbb{A} + \mathbb{B}(U)) U = F, \quad (13)$$

where $\mathbb{A} = \{a_{ij}\}_{i,j=1}^N$ is the stiffness matrix obtained using \mathbb{P}_1 finite elements, $\mathbb{B}(U) = \{b_{ij}(U)\}_{i,j=1}^N$ is the stabilization matrix, and $F = \{f_i\}_{i=1}^N$ is the discretized right-hand side.

Instead of solving this nonlinear system directly, we solve the modified system

$$\begin{aligned} (\mathbb{A} + \mathbb{D}) \tilde{U}^\nu &= F - (\mathbb{D} + \mathbb{B}(U^{\nu-1})) U^{\nu-1}, & \nu \geq 1, \\ U^\nu &= \omega \tilde{U}^\nu + (1 - \omega) U^{\nu-1}, \end{aligned} \quad (14)$$

where $\mathbb{D} = \{d_{ij}\}_{i,j=1}^N$ is the artificial diffusion matrix (see Eq. (5)), ω is a damping parameter, and ν denotes the ν^{th} iteration step.

The rationale for solving the modified system is that the matrix $\mathbb{A} + \mathbb{D}$ is a constant M-matrix of non-negative type. Hence, it can be factorized once, stored, and reused within the iterative loop, resulting in computational efficiency.

If Eq. (1) is nonlinear, then the matrix \mathbb{A} also becomes nonlinear, and we directly solve Eq. (13). This approach is referred to as the *fixed-point matrix* strategy in [24]. In this case too, we employ a dynamic damping parameter ω . The stopping criterion is either a maximum of 10^4 nonlinear iterations or when the ℓ_2 norm of the residual falls below $10^{-8} \sqrt{\#\text{dofs}}$, where $\#\text{dofs}$ denotes the total number of degrees of freedom.

- **ESTIMATE:** To estimate the error in each mesh cell K , we use the global upper bound η presented in Theorem 4. We observe that the estimator includes certain constants. For simplicity, we set C_I , C_F , C , and C_{inv} to unity. The constant $C_{\text{edge,max}}$ is computable for 2D triangular elements and is given by

$$C_{\text{edge,max}} = \frac{4\sqrt{2} (1 + \sqrt{2}) |K|}{1 - C_{\cos} \rho_K^3},$$

where ρ_K is the diameter of the largest ball inscribed in K , $|K|$ is the area of the element K , and $C_{\cos} \geq \cos(\theta_i)$ for $i = 1, 2, 3$, with θ_i denoting the angle opposite the edge E_i of the triangle K (see [21]).

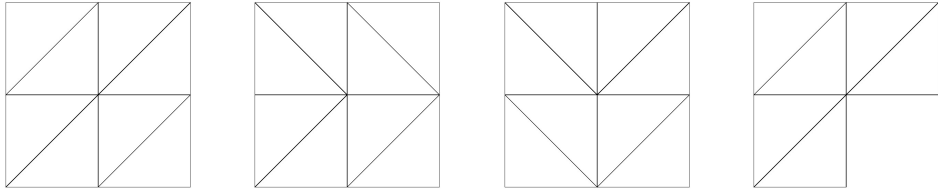


Figure 1: Coarsest grids for the numerical studies, Grid 1,2,3,4 (left to right)

- **MARK:** For marking mesh cells, we use the maximum strategy, also known as Dörfler marking [15]. A common issue that arises when marking mesh cells in convection-dominated problems is that only a few cells with high error are marked, which deteriorates the effectiveness of the adaptive algorithm.

To overcome this, we adopt a dual marking strategy: in addition to the maximum strategy, we enforce a minimum percentage of mesh cells that must be refined, as suggested in [28]. This strategy involves two parameters: `ref_tol` and `min_ref`.

Let $\eta_{\max} = \max_{K \in \mathcal{T}_h} \eta_K$. A mesh cell K is marked for refinement if

$$\eta_K \geq \text{ref_tol} \cdot \eta_{\max}.$$

If at least `min_ref` fraction of the cells are marked, the process is complete. Otherwise, we relax `ref_tol` by multiplying it by a factor of 0.8 and repeat the marking process.

In our numerical studies, we set `ref_tol` = 0.5 and `min_ref` = 0.05, corresponding to marking at least 5% of the cells.

- **REFINE:** For mesh refinement, we follow the red-green refinement process [44]. A grid with red-green refinement consists of regularly refined cells arising from red refinement and closure cells originating from green refinement. Both cell types may be marked for refinement by the error indicator.

In the first step of the refinement process, the parents of closure cells are marked for refinement if any of their children are marked. Note that the parents of closure cells are regularly refined cells from a coarser grid. All closure cells are then removed so that only regularly refined cells remain, and all marked cells are refined using regular refinement. Finally, the resulting grid is closed.

An alternative approach is to use grids with hanging nodes. Theoretical and numerical results regarding such grids were presented in [26]. It was shown that the AFC scheme with the Kuzmin limiter fails to satisfy the discrete maximum principle (DMP) on grids refined with red-green refinement, whereas all other methods satisfy the DMP on both red-green refined grids and grids with hanging nodes. However, the error estimates and performance of the nonlinear loop remained comparable for both refinement strategies.

Therefore, in this work, unless otherwise mentioned, we present results only using grids refined via red-green refinement.

To ensure a fair comparison of the results, we terminate the adaptive loop once the total number of degrees of freedom reaches 2.5×10^5 . For problems defined on $(0, 1)^2$ we consider three different types of grids, whose level-0 configurations are shown in Fig. 1 (see Grid 1,2,3). Grid 4 corresponds to the L-shaped domain $[0, 1]^2 \setminus [0.5, 1] \times [0, 0.5]$.

For our adaptive algorithm, we begin with two uniform refinement steps, then proceed to adaptive refinement. The resulting systems of equations are solved using the sparse direct solver UMFPACK [13]. All simulations were carried out using the finite element library PARMOOON [45].

The numerical assessment is performed based on the following criteria:

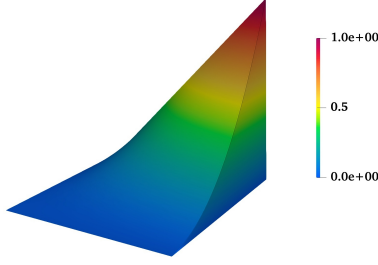


Figure 2: Example 4.1: Numerical solution with the MUAS method on Grid 1 with 16641 degrees of freedom.

1. **Effectivity index:** The effectivity index provides a measure of the performance of the error estimator. It is defined as

$$\gamma_{\text{eff}} = \frac{\eta}{\|u - u_h\|_a}. \quad (15)$$

Ideally, we seek $\gamma_{\text{eff}} \approx 1$, independently of the choice of ε (robustness).

2. **Accuracy of the solution:** Plots of the error in the solution and the gradient of the error in the L^2 norm are presented.
3. **Sharpness of the layer:** The thickness of the interior layer is plotted against the total number of degrees of freedom (#dofs). For this, we compute

$$\text{smear}_{\text{int}} = y_2 - y_1, \quad (16)$$

along $x = a$, where y_1 is the y -coordinate of the first point on the cut line (a, y_1) with $u_h(a, y_1) \geq 0.1$ and y_2 is the y -coordinate of the first point with $u_h(a, y_2) \geq 0.9$.

4. **Quality of the adaptively refined grids:** Visual representations of the solution and the corresponding adaptively refined grids are presented.
5. **Efficiency of the nonlinear solver:** Since the algebraic stabilization schemes are nonlinear in nature, we plot the number of iterations and rejections with respect to the total #dofs. As the computational cost of a rejection in the nonlinear loop is equivalent to that of an iteration, both are plotted for comparison.
6. **Computational cost:** The total time taken to solve the problem is reported.

4.1 Solution with Regular Boundary Layer

Consider Eq. (1) with $\varepsilon = 10^{-2}$, $\mathbf{b} = (2, 3)^\top$, $c = 1$, $\Omega = (0, 1)^2$, and $\Gamma_D = \Gamma$. The right-hand side and the Dirichlet boundary condition are chosen such that

$$u(x, y) = xy^2 - y^2 \exp\left(\frac{2(x-1)}{\varepsilon}\right) - x \exp\left(\frac{3(y-1)}{\varepsilon}\right) + \exp\left(\frac{2(x-1) + 3(y-1)}{\varepsilon}\right)$$

is the exact solution; see Fig. 2. The solution exhibits regular boundary layers along the outflow boundaries $x = 1$ and $y = 1$.

We use this example to evaluate both the effectivity index and the accuracy of the numerical solution. Fig. 3 plots the effectivity index for Grids 1, 2, and 3. The effectivity index for the MC limiter is the largest, approaching 20, whereas for all other methods, the values are comparable and close to 12 on sufficiently refined grids. Furthermore, we observe robustness with respect to the choice of grid.

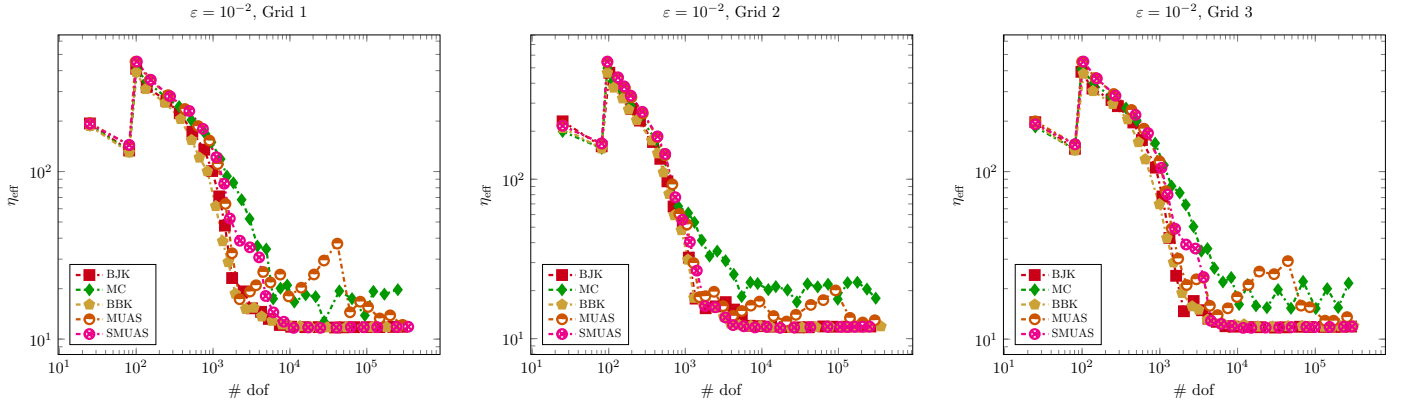


Figure 3: Example 4.1: Effectivity index for Grids 1–3 (left to right).

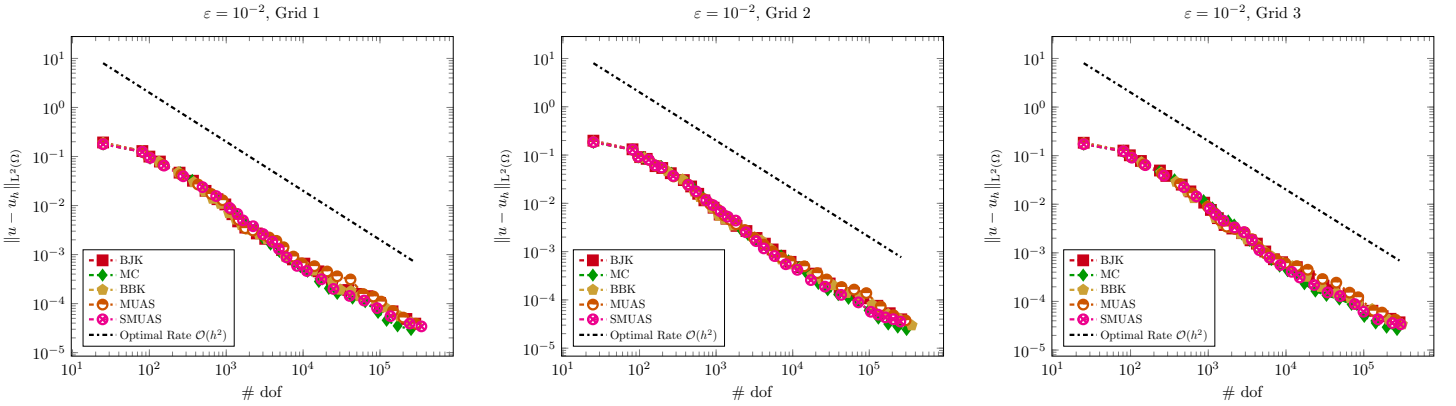


Figure 4: Example 4.1: Error in the $L^2(\Omega)$ norm for Grids 1–3 (left to right).

Figs. 4 and 5 show the L^2 error of the solution and the L^2 error of its gradient, respectively. We observe that all limiters exhibit optimal convergence rates for all three grids.

Next, we investigate the decay of η_3 , the term arising from the stabilization part. In Fig. 6, we observe

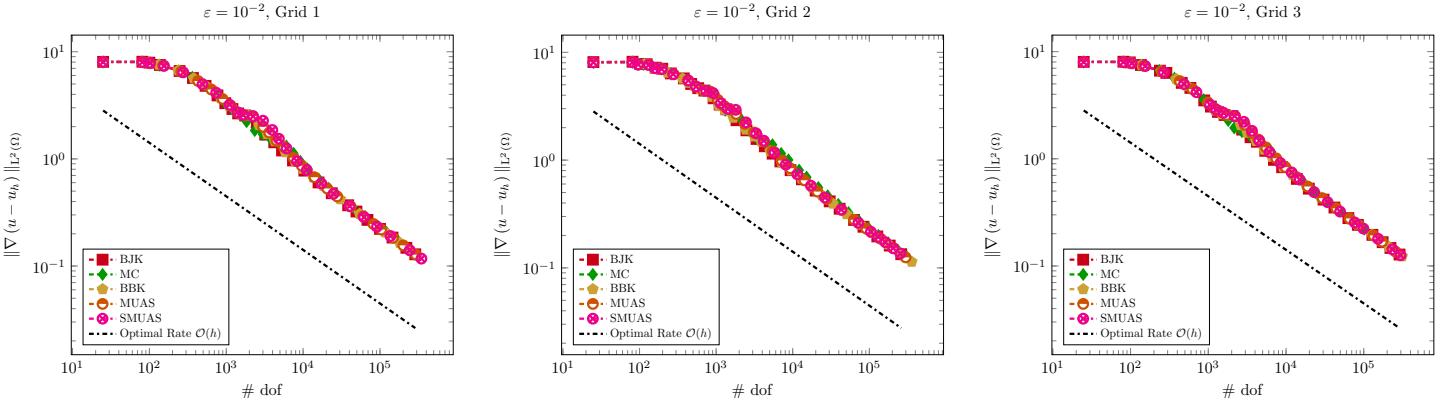


Figure 5: Example 4.1: Error of the gradient in the $L^2(\Omega)$ norm for Grids 1–3 (left to right).

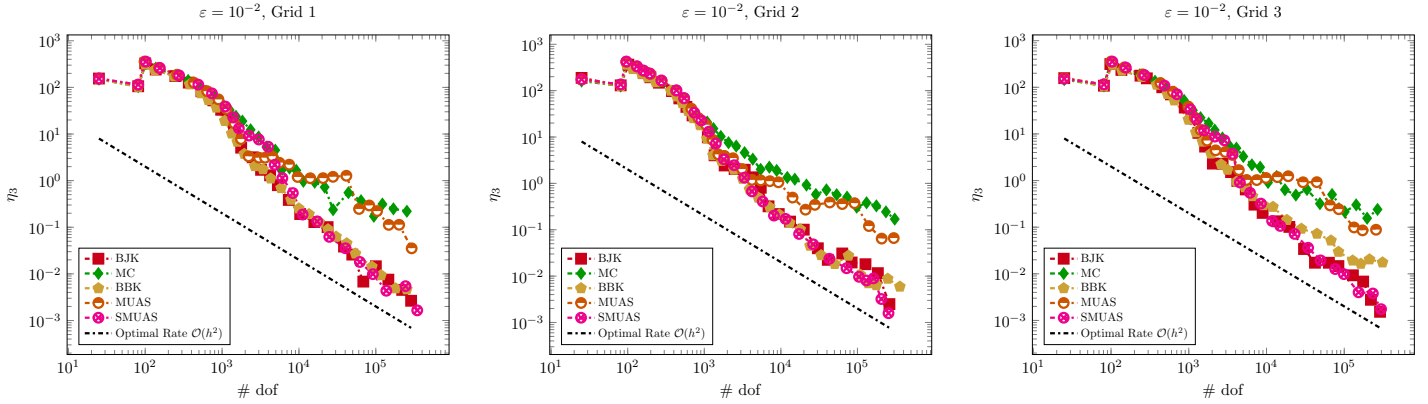


Figure 6: Example 4.1: Values of η_3 for Grids 1–3 (left to right).

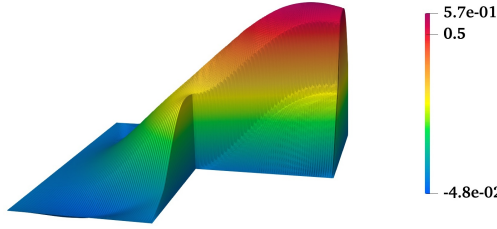


Figure 7: Example 4.2: Numerical solution obtained with algebraic stabilization and the MUAS limiter on Grid 4 with 49,655 degrees of freedom.

that η_3 decays at a rate of $\mathcal{O}(h^2)$ for all methods except the monolithic and MUAS limiters. This deterioration is independent of the choice of grid. Although the convergence rate of η_3 deteriorates on sufficiently refined meshes, this behaviour does not adversely affect the accuracy of the solution itself. One of the motivations for the SMUAS method was to achieve optimal convergence on arbitrary grids [34], and here we clearly see that SMUAS outperforms the MUAS method.

From this example, we conclude that the a posteriori error estimator delivers comparable results across all limiters and is robust with respect to the choice of grid. Based on this example, the BJK, BBK, and the MUAS method seem to be the most promising.

4.2 Solution with Corner Singularity on L-shaped Domain

Consider Eq. (1) on the L-shaped domain

$$\Omega = (0, 1)^2 \setminus [0.5, 1] \times [0, 0.5].$$

The coefficients are given by

$$\varepsilon = 10^{-6}, \quad \mathbf{b} = (3, 1)^\top, \quad c = 1, \quad f = 100 r(r - 0.5)(r - \sqrt{2}/2),$$

where

$$r = \sqrt{(x - 0.5)^2 + (y - 0.5)^2}.$$

The entire boundary is subject to Dirichlet conditions, i.e., $\Gamma_D = \Gamma$, with boundary data $u_D = 0$ (see Fig. 7).

An analytical solution to this problem is not known. Nevertheless, the solution exhibits several characteristic features:

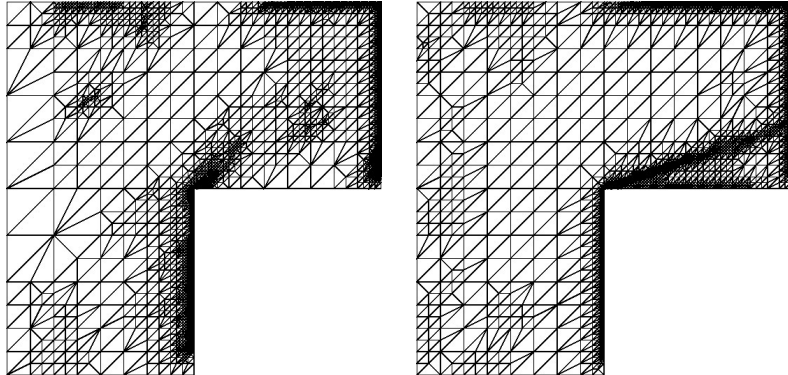


Figure 8: Example 4.2: Adaptive grids for the AFC methods with $\#dofs \approx 2.5 \times 10^5$. BJK limiter (left) and MC limiter (right).

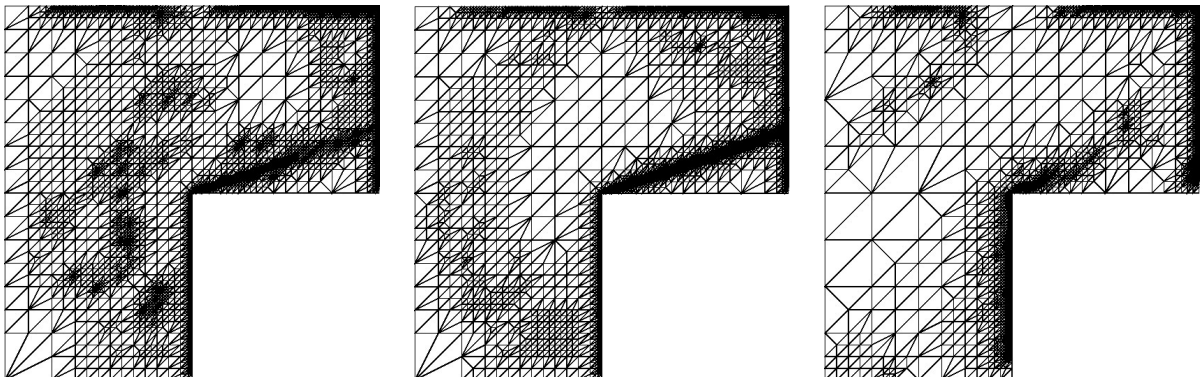


Figure 9: Example 4.2: Adaptive grids for the algebraically stabilized methods with $\#dofs \approx 2 \times 10^5$. MUAS (left), SMUAS (middle), and BBK (right).

- a corner singularity at the re-entrant point $(0.5, 0.5)$,
- an interior layer aligned with the convection direction,
- boundary layers along the top boundary $y = 1$ and along the vertical segments

$$\{(0.5, y) : 0 < y \leq 0.5\}, \quad \{(1, y) : 0.5 < y \leq 1\}.$$

Due to the presence of the re-entrant corner, the solution does not belong to $H^2(\Omega)$. The adaptively refined grids obtained with all limiters are shown in Fig. 8 and Fig. 9 for $\#dofs \approx 2.5 \times 10^5$. Among the AFC schemes, the BJK limiter fails to adequately refine the interior layer; instead, most refinement is concentrated near the boundary layers and the re-entrant corner. In contrast, the MC limiter performs better, resolving both the boundary layers and the interior layer more effectively.

For the algebraically stabilized schemes, the MUAS and SMUAS methods provide the best grid adaptation, with the SMUAS method performing slightly better overall. The BBK method struggles to adequately refine the interior region. In comparison with the AFC schemes, the SMUAS method appears to be the most promising in terms of adaptive grid quality.

Figure 10 displays the number of iterations and rejections in the nonlinear iterative loop. The left y -axis corresponds to the BJK limiter, while the right y -axis corresponds to the remaining limiters. Clearly, the BJK limiter performs the worst among the tested methods, whereas the MUAS and SMUAS limiters achieve the best results. Similar observations for the BJK limiter under uniform refinement were reported in [24].

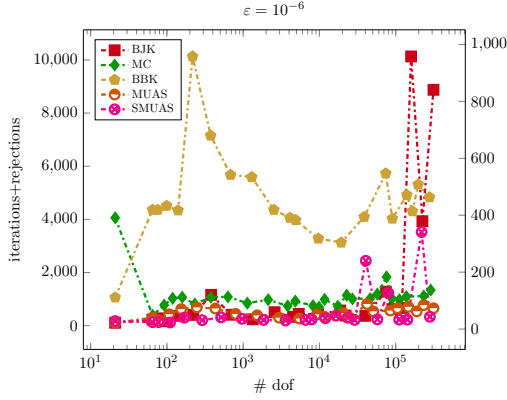


Figure 10: Example 4.2: Number of iterations and rejections. The left y -axis corresponds to the BJK limiter, whereas the right y -axis corresponds to the other limiters.

Limiter	Time (s)	Number of Adaptive Loops
BJK	1947	22
MC	150	26
BBK	265	21
MUAS	136	23
SMUAS	3345	23

Table 1: Example 4.2: Computing time (in seconds) and number of adaptive loops for the adaptive algorithm.

Table 1 reports the computing time and the number of adaptive loops required by the adaptive algorithm. We observe that the MUAS method is the most efficient, whereas the SMUAS method is the least efficient. In fact, SMUAS requires approximately twice as much computing time as the next most inefficient method (BJK). Hence, although the SMUAS method requires the fewest adaptive loops, it is inefficient in terms of overall computing time.

Overall, in terms of adaptive grid quality, the SMUAS and MC limiters perform best, whereas in terms of nonlinear iteration efficiency, the MUAS and SMUAS methods yield the most favorable results. Regarding computing time, MUAS and the MC limiter take the least time. In both respects, the BJK limiter is the weakest performer among the tested methods.

4.3 Solution with Different Regimes

This example is taken from [9]. The domain contains regions where convection dominates, regions where reaction dominates, and regions where diffusion is the primary mechanism.

Consider Eq. (1) on $\Omega = (0, 1)^2$ with $\varepsilon = 10^{-6}$, $f = 0$, and a convective field given by

$$\mathbf{b}(x, y) = r \psi(r) \begin{bmatrix} y + 27/16 \\ 1 - x \end{bmatrix}, \quad r = \left((x - 1)^2 + (y + \frac{27}{16})^2 \right)^{1/2},$$

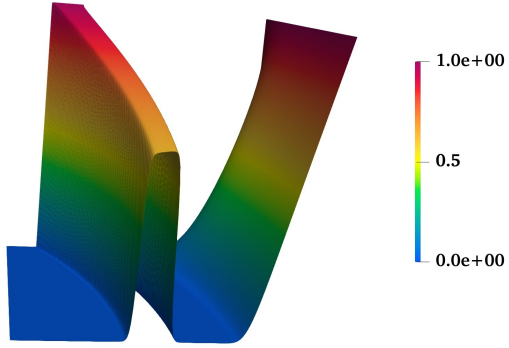


Figure 11: Example 4.2: Numerical solution with algebraic stabilisation and MUAS limiter on Grid 1 with 66049 degrees of freedom.

where

$$\psi(r) = \begin{cases} \frac{1}{r}, & |r - r_0| \leq r_d, \\ \frac{1}{r_0 + r_d} \exp(-1000(r - (r_0 + r_d))^2), & r > r_0 + r_d, \\ \frac{1}{r_0 - r_d} \exp(-1000(r - (r_0 - r_d))^2), & r < r_0 - r_d, \end{cases}$$

with $r_0 = 17/8$ and $r_d = \sqrt{1217}/16 - r_0$.

The reaction coefficient is defined analogously:

$$c = \begin{cases} 1, & |r - r_0| \leq r_d, \\ \exp(-100(r - (r_0 + r_d))^2), & r > r_0 + r_d, \\ \exp(-100(r - (r_0 - r_d))^2), & r < r_0 - r_d. \end{cases}$$

Both the convection and reaction fields attain their largest values in the region

$$\{(x, y) \in \Omega : |r - r_0| \leq r_d\},$$

and decay exponentially away from it, with the reaction field decaying more slowly (see Fig. 11).

Homogeneous Neumann boundary conditions are imposed along the boundary $(1, y)$ for $y \in (0, 1)$. Dirichlet boundary conditions on the remaining boundary are prescribed as

$$u_D = \begin{cases} 0, & y = 0, \\ 0, & x = 0, y \in [0, 0.125), \\ 1, & x = 0, y \in [0.125, 0.25], \\ 0, & x = 0, y \in (0.25, 1), \\ 1, & y = 1. \end{cases}$$

All simulations are performed on Grid 1. To assess the quality of the numerical solution, we compare solution values along several cutlines:

$$x = 0.5, \quad x = 1, \quad x = y, \quad x = 1 - y.$$

In Fig. 12 we present the results along the cutline $x = 1$ for two degrees-of-freedom levels: approximately 100 (left), and 125,000 (right). The solution obtained with 100 # dof is the solution on the first adaptively

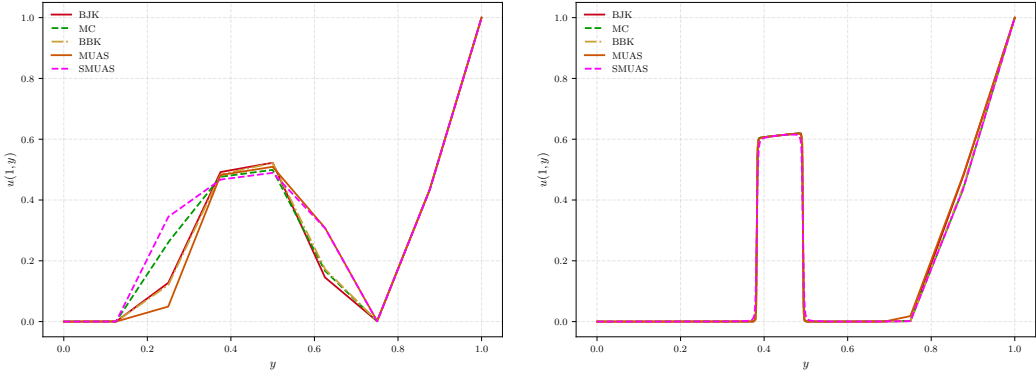


Figure 12: Example 4.3: Solution along the cutline $x = 1$ with approximately 100 # dof (left) and 125,000 # dof (right).

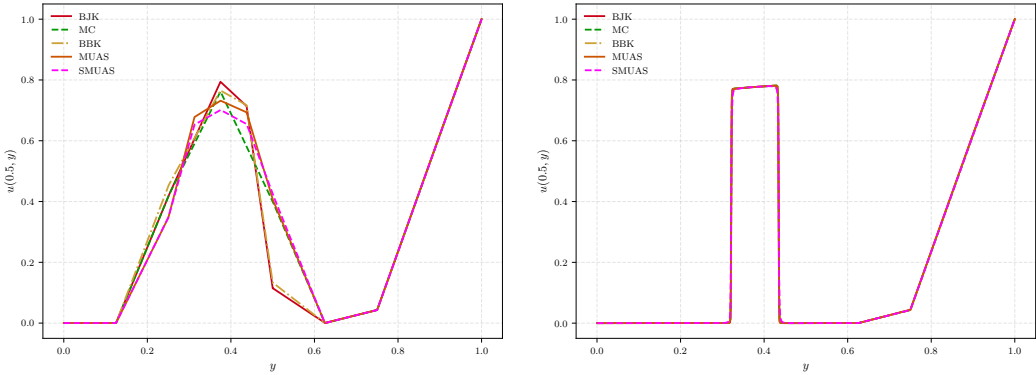


Figure 13: Example 4.3: Solution along the cutline $x = 0.5$ with approximately 100 # dof (left) and 125,000 # dof (right).

refined grid. Here we see that all the limiters capture the basic features of the example. As the mesh becomes fine, we observe that the solution is robust with respect to the choice of limiter, and only minimal (if any) differences are visible in the solution profiles.

Figs. 13, 14, and Fig. 15 shows the results along the cutline $x = 0.5$, $x = y$, and $x = 1 - y$, respectively. Here, similar observations can be made: the limiters produce nearly identical solution profiles, indicating that the method behaves robustly in all the configurations.

Lastly, in Figs. 16 and 17, we present the adaptive grids obtained using different limiters for approximately 2.5×10^5 degrees of freedom. We observe that the layers captured by the MC limiter are sharper than those produced by the BJK limiter; however, the MC limiter tends to over-refine the mesh near the inlet boundary ($y = 0$).

Among the algebraically stabilized methods, the SMUAS method appears to be the most promising, with the BBK method showing comparable performance. Overall, the quality of the adaptive grids is similar across the considered approaches, with the BJK and SMUAS methods providing the most favorable results.

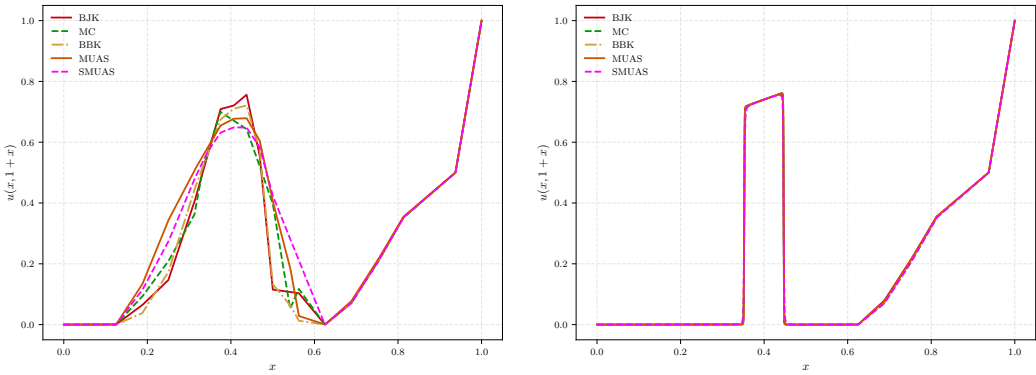


Figure 14: Example 4.3: Solution along the cutline $x = 1 - y$ with approximately 100 # dof (left) and 125,000 # dof (right).

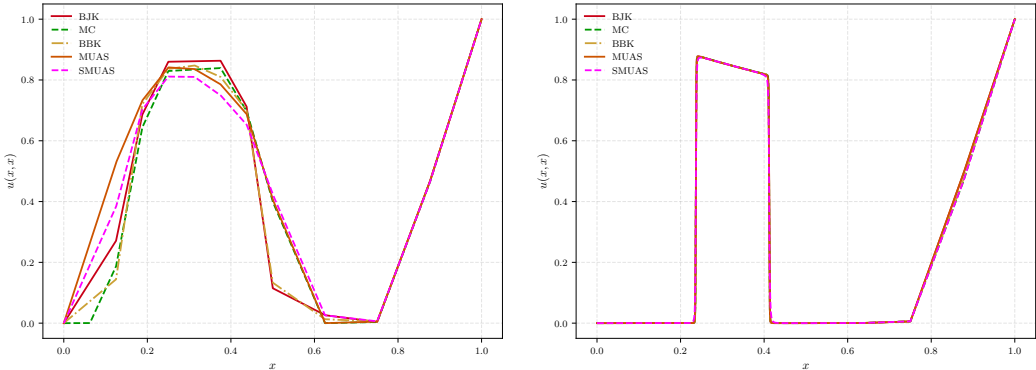


Figure 15: Example 4.3: Solution along the cutline $x = y$ with approximately 100 # dof (left) and 125,000 # dof (right).

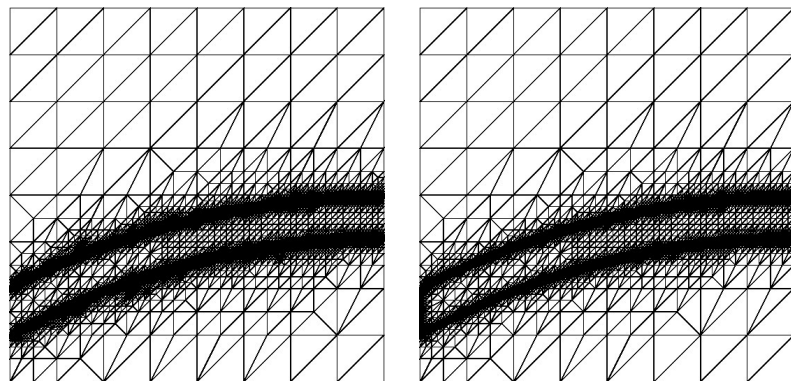


Figure 16: Example 4.3: Adaptive grids for the AFC methods with $\# \text{ dofs} \approx 2.5 \times 10^5$. BJK limiter (left) and MC limiter (right).

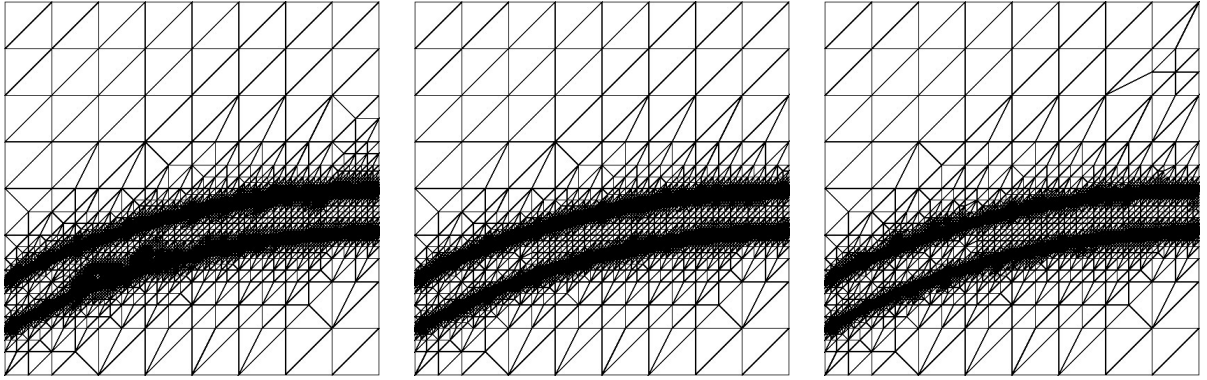


Figure 17: Example 4.3: Adaptive grids for the algebraically stabilized methods with $\# \text{ dofs} \approx 2 \times 10^5$. MUAS (left), SMUAS (middle), BBK (right).

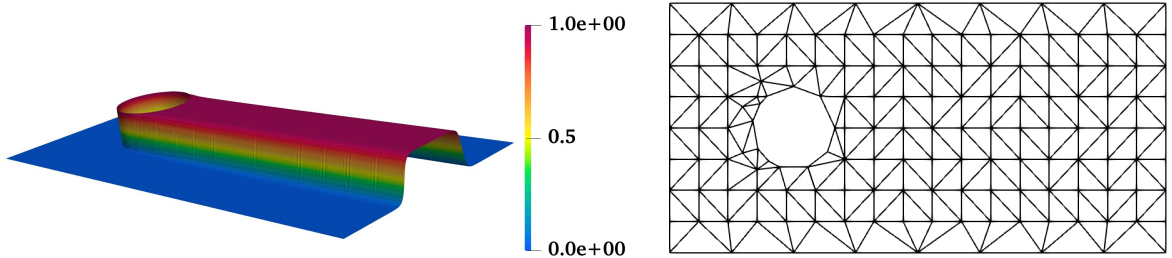


Figure 18: Example 4.4: Solution for $\varepsilon = 10^{-4}$ (left), computed with the MUAS limiter using 33,496 degrees of freedom; initial grid (right), level 0.

4.4 Hemker Problem

The next example we consider is the standard Hemker problem, originally introduced in [19]. The computational domain is given by

$$\Omega = (-3, 9) \times (-3, 3) \setminus \{(x, y) \in \mathbb{R}^2 : x^2 + y^2 \leq 1\}.$$

The convection field is prescribed as $\mathbf{b} = (1, 0)^\top$, while the reaction coefficient and the right-hand side in Eq. (1) vanish, i.e.,

$$c = f = 0.$$

Dirichlet boundary conditions are imposed at $x = -3$, where $u_D = 0$, and on the circular boundary, where $u_D = 1$. On all remaining boundaries, homogeneous Neumann boundary conditions are prescribed.

This problem was studied comprehensively in [3] for $\varepsilon = 10^{-4}$, where reference values for several quantities of interest were reported. The same diffusion parameter is employed in our study. Figure 18 (left) illustrates the solution, which takes values in the interval $[0, 1]$, while Figure 18 (right) shows the initial grid with $\# \text{dof} = 151$.

Although the exact solution to this problem is unknown, several quantities of interest are available. In particular, the solution is known to be bounded between 0 and 1, and reference values exist for the smearing of the internal layer along the cutline $x = 4$. To quantify these properties, we introduce the measures

$$\text{osc}(u_h) = \max(u_h) - \min(u_h) \approx 1,$$

and

$$\text{smear}_{\text{int}} = y_2 - y_1,$$

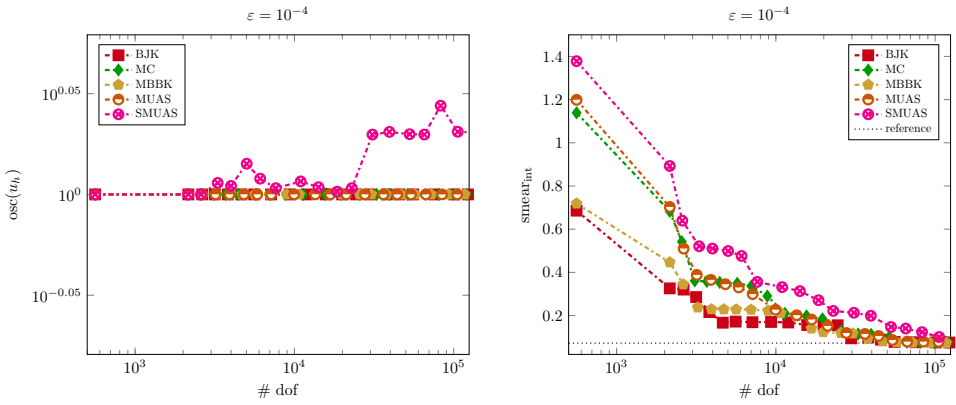


Figure 19: Example 4.4: Spurious oscillations for different limiters (left), thickness of the internal layer along the cutline $x = 4$ (right).

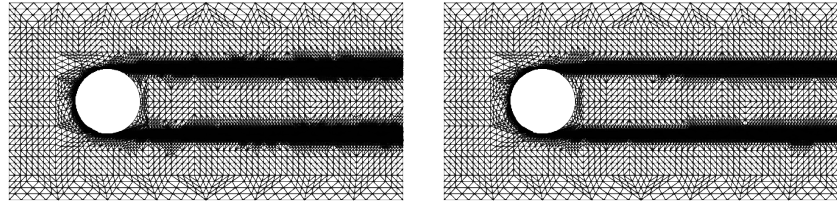


Figure 20: Example 4.4: Adaptive grids for the AFC methods with $\#\text{dofs} \approx 10^5$. BJK limiter (left) and MC limiter (right).

(see Eq. (16)). The cutline is discretised using 100,000 equidistant intervals, and the discrete solution is evaluated at the corresponding nodes.

Figure 19 (left) presents the oscillation measure. We observe that all methods, except the SMUAS limiter, satisfy the DMP. With mesh refinement, the grids become partially non-Delaunay. As noted in [9], the MC limiter requires a Delaunay triangulation to guarantee the DMP; however, in the present setting, this condition is not violated. This can be explained by the adaptive refinement, where only local portions of the mesh are non-Delaunay, which still allows the DMP to hold in practice. A closer inspection of the numerical solution shows that the violations produced by the SMUAS method occur primarily in the vicinity of the circular obstacle. The SMUAS limiter relies on a reconstructed state u_{ij} based on a recovered gradient of the numerical solution. In the Hemker problem, the solution contains very sharp layers around the obstacle and along the convection direction, and these layers are not aligned with the mesh. Consequently, the reconstructed gradient may not accurately represent the local behaviour of the solution near the layer and the limiter introduces insufficient artificial diffusion in some regions, leading to mild over- and undershoots.

Figure 19 (right) shows the smearing of the internal layer. A reference value of 0.0723 is reported in [3]. The BJK limiter provides the sharpest resolution of the layer, followed closely by the BBK limiter. For sufficiently fine meshes, all limiters approach values close to the reference result, although the SMUAS method exhibits the largest amount of smearing.

Finally, Figures 20 and 21 present the adaptive grids obtained for all methods using approximately $\#\text{dofs} \approx 10^5$. For the AFC methods, the MC limiter yields the sharpest internal layer, whereas for the algebraically stabilised schemes, the MUAS and BBK methods provide the best resolution.

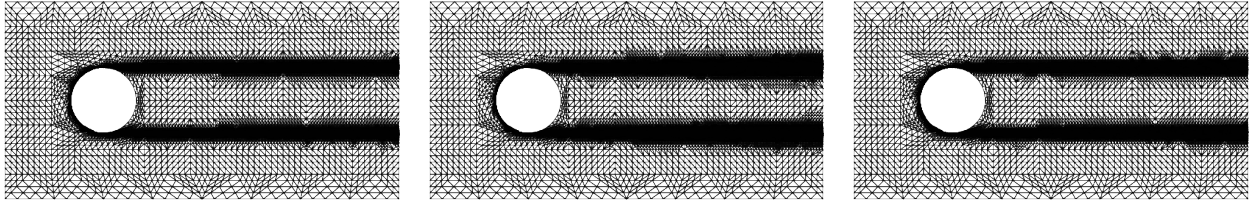


Figure 21: Example 4.4: Adaptive grids for the algebraically stabilised methods with $\#\text{dofs} \approx 10^5$. MUAS (left), SMUAS (middle), BBK (right).

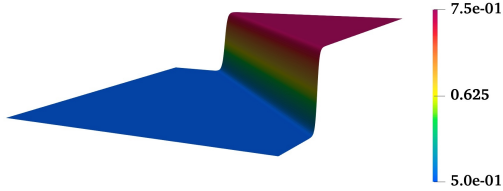


Figure 22: Example 4.5: Numerical solution obtained with the AFC scheme and BJK limiter on Grid 1 with 16,641 degrees of freedom.

4.5 Solution with Inner Layer, Non-Linear Convection and Linear Reaction

Consider Eq. (1) with

$$\varepsilon = 10^{-3}, \quad \mathbf{b} = (u, u)^\top, \quad c = 0, \quad \Omega = (0, 1)^2, \quad \Gamma_D = \Gamma.$$

The right-hand side and boundary conditions are chosen such that

$$u(x, y) = \frac{3}{4} - \frac{1}{4 \left[1 + \exp \left(\frac{-4x+4y-1}{32\varepsilon} \right) \right]}$$

is the exact solution (see Fig. 22). This is a non-linear example, with the non-linearity arising from the convection term. Equation (2) is still satisfied in this case. An interior layer develops along the line $-4x + 4y - 1 = 0$. Among the three grids, Grid 1 is aligned with this interior layer. This example serves as the steady-state counterpart of Example 2 from [47].

Fig. 23 presents the effectivity index. For Grid 1, the values obtained for all methods on sufficiently fine meshes are close and approximately equal to 16. The decay is smooth for most limiters, whereas the MC limiter exhibits several noticeable jumps. On Grids 2 and 3, this behaviour becomes more pronounced. For these grids, the effectivity index for all methods except the BJK limiter approaches values around 4, while the BJK limiter remains closer to 10.

This behaviour can be attributed to the nonlinear nature of the problem. In this example, the convection field depends on the solution itself, $\mathbf{b} = (u, u)^\top$, and hence the effective transport direction changes during the nonlinear iteration. On Grid 1, the interior layer is approximately aligned with the mesh, and therefore all methods achieve similar estimator behaviour. On Grids 2 and 3, however, the layer is not aligned with the mesh, which makes the stabilization more sensitive to the limiter. The BJK limiter enforces stronger upwinding and therefore reacts more robustly to the moving transport direction, whereas the other limiters reduce artificial diffusion and consequently produce smaller estimator values. The jumps observed for the MC limiter occur when the limiter switches between active and inactive states during the adaptive refinement, which causes abrupt changes in the stabilization contribution to the residual.

Figs. 24 and 25 show the L^2 error of the solution and the L^2 error of its gradient, respectively. For Grid 1, the error decays optimally for all methods. In contrast, on Grids 2 and 3, all methods except the BJK and MC limiters lose their optimal convergence rate. This again reflects the influence of mesh alignment. Since

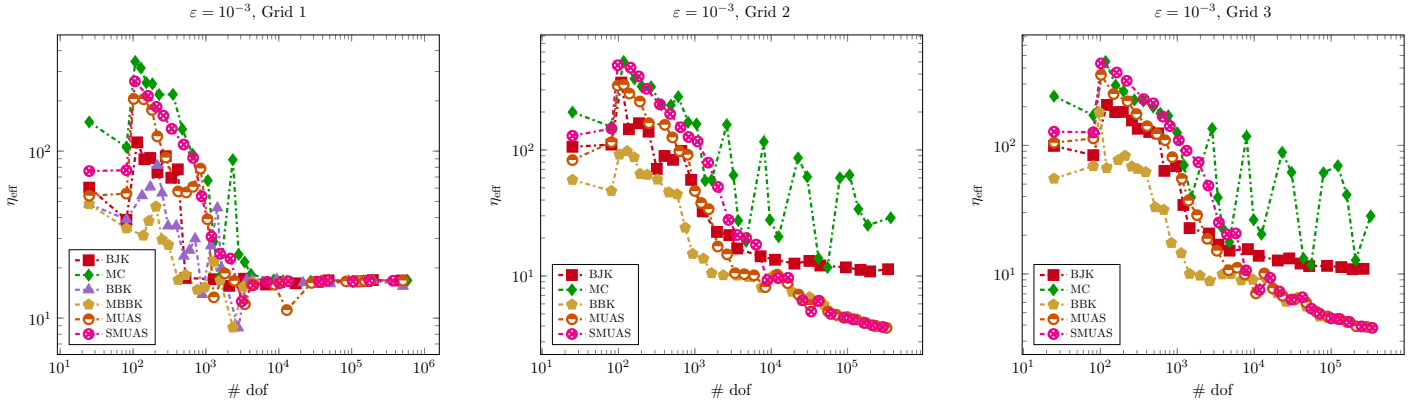


Figure 23: Example 4.5: Effectivity index for Grids 1–3 (left to right).

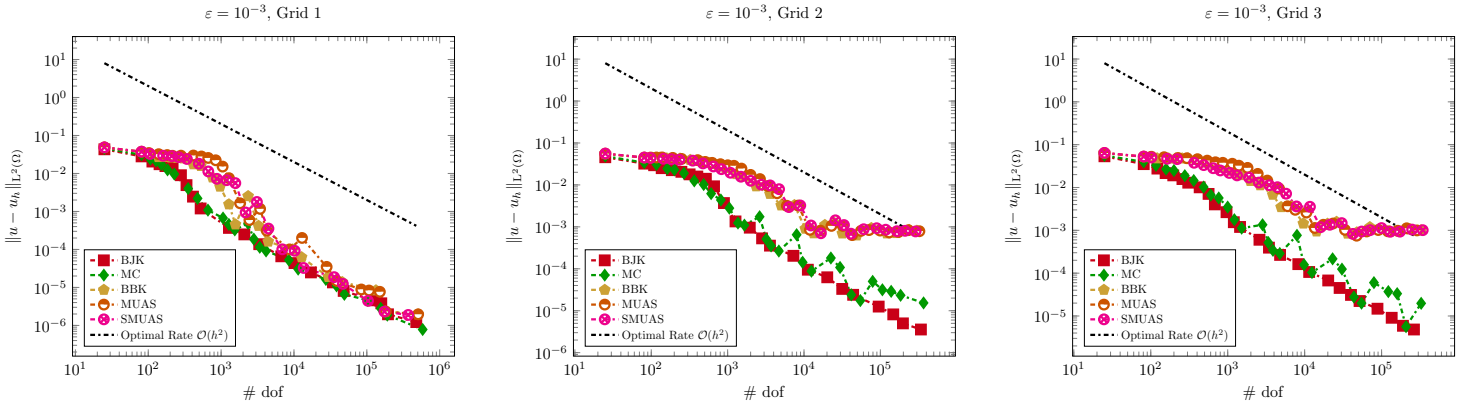


Figure 24: Example 4.5: Error in the $L^2(\Omega)$ norm for Grids 1–3 (left to right).

the location and orientation of the interior layer depend on the solution, the problem resembles a transport-dominated equation with a moving layer. The stronger upwinding behaviour of the BJK limiter allows it to capture this layer more accurately on non-aligned meshes and therefore yields the most accurate results in this example.

We also note that, in contrast to the Hemker problem, all limiters satisfy the discrete maximum principle for this test case. The numerical solution remains bounded within the physically relevant range $[0.5, 0.75]$ for all meshes and all methods.

Figure 26 shows the number of iterations and rejections obtained using the *fixed-point matrix* method. The BBK, MUAS, and SMUAS limiters require the smallest number of nonlinear iterations across all grids, whereas the BJK limiter performs the worst. In contrast, the algebraic stabilization methods depend on smoother indicators and therefore lead to a more stable nonlinear iteration. Consequently, algebraically stabilized schemes are more efficient from the solver perspective for nonlinear problems.

Figs. 27 and 28 show the adaptively refined grids for the AFC and algebraically stabilized methods, respectively. Among the AFC approaches, the BJK limiter resolves the interior layer most sharply. Among the algebraically stabilized methods, the BBK limiter appears most effective, although all methods exhibit some degree of over-refinement near the top-right corner where the layer terminates.

Finally, the computing times are reported in Table 2. The BBK limiter is the most efficient overall, while the MC and MUAS limiters also show good performance. In contrast, the SMUAS method is significantly more expensive, requiring approximately twenty-six times more computational time than the next slowest

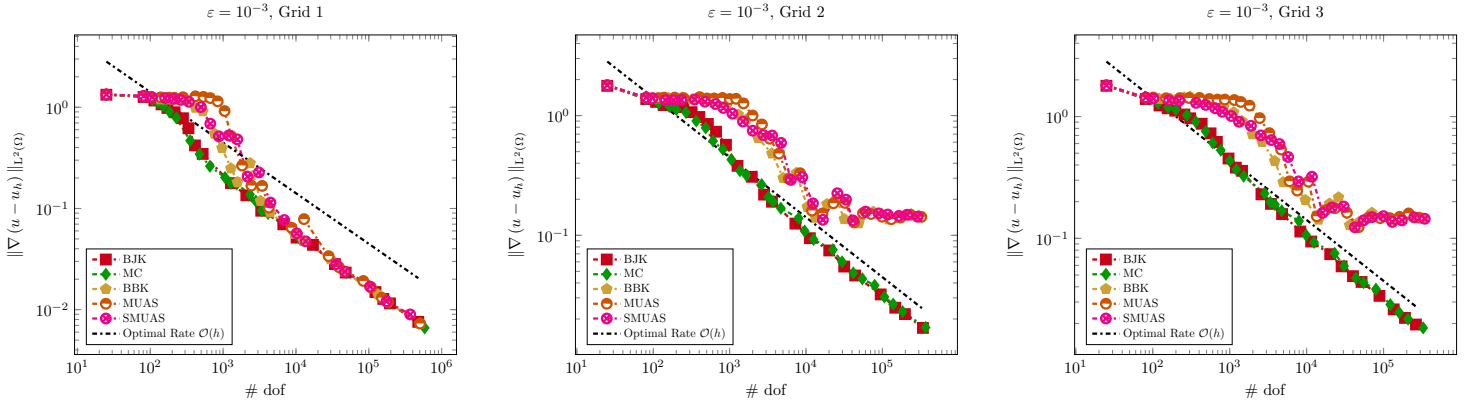


Figure 25: Example 4.5: Error of the gradient in the $L^2(\Omega)$ norm for Grids 1–3 (left to right).

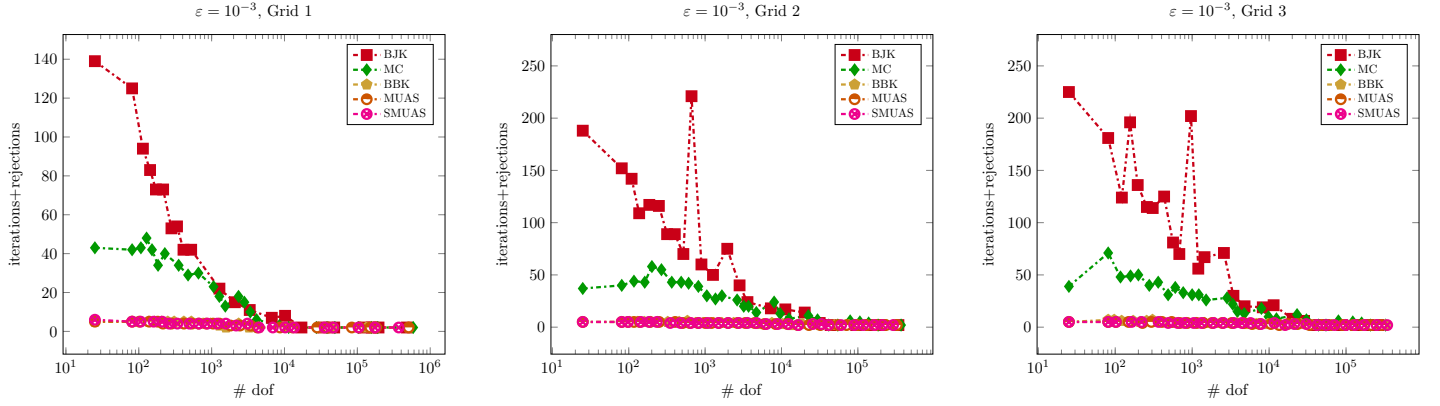


Figure 26: Example 4.5: Number of iterations and rejections for Grids 1–3 (left to right).

method. This high cost arises from the use of reconstructed states involving fictitious points and gradient evaluations, which must be performed repeatedly as the mesh is refined. Overall, the BBK method provides the best balance between accuracy and computational efficiency for this nonlinear example.

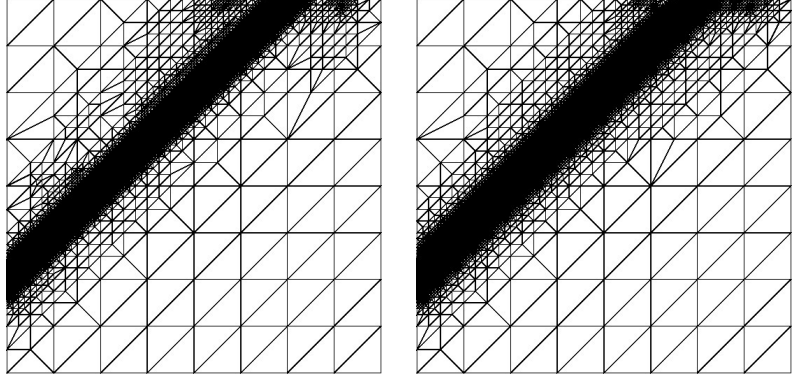


Figure 27: Example 4.5 Adaptive grids for the AFC methods with $\# \text{ dofs} \approx 2.5 \times 10^5$. BJK limiter (left) and MC limiter (right).

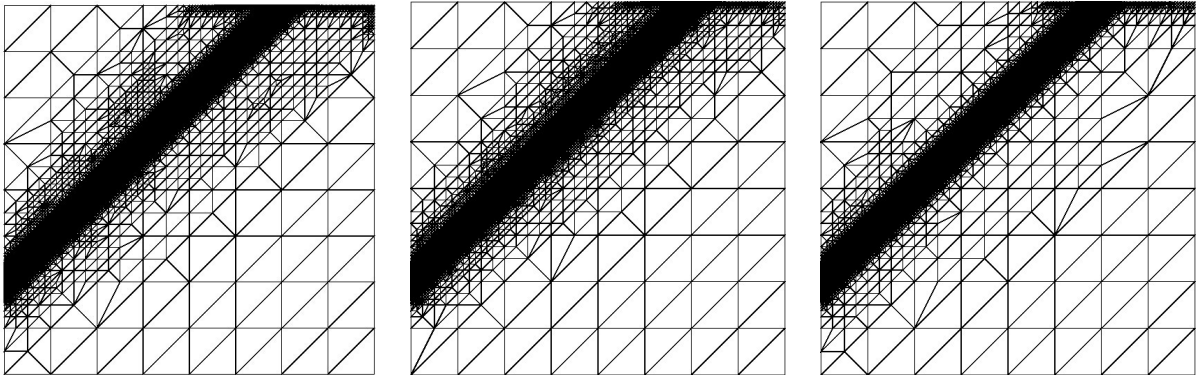


Figure 28: Example 4.5 Adaptive grids for the algebraic stabilized methods with $\# \text{ dofs} \approx 2.5 \times 10^5$. MUAS (left), SMUAS (middle), BBK (right).

Limiter	Time (s)	Number of Adaptive Loops
BJK	190	22
MC	205	26
BBK	160	23
MUAS	193	26
SMUAS	5025	24

Table 2: Example 4.5: Computing time for the adaptive algorithm (in seconds) and the number of adaptive loops for Grid 1.

5 Summary

In this section, we summarize the results presented throughout the paper. We investigated the numerical behaviour of several limiting strategies on adaptively refined meshes. In particular, we considered AFC schemes with the BJK and MC limiters and algebraically stabilized schemes, including MUAS, SMUAS, and the BBK method. The numerical assessment is organized into three categories.

1. **Accuracy:** We evaluate accuracy using both the effectivity index and the error in the numerical solution.

From Example 4.1, all methods achieve optimal convergence rates. The BJK, BBK, and SMUAS methods produce the smallest effectivity indices, while differences in the actual error remain minor.

In the nonlinear Example 4.5, the behaviour changes. The transport direction depends on the solution, and the interior layer is not aligned with the mesh on Grids 2 and 3. In this case, the BJK limiter retains the most accurate solution, while the remaining methods experience a loss of optimal convergence. The MC limiter also performs robustly, whereas the algebraically stabilized methods yield slightly larger errors. Overall, the BJK limiter provides the most reliable accuracy across all tests.

2. **Approximation:** Here, we consider both the sharpness of internal layers and the quality of adaptive mesh refinement.

In Example 4.2, the SMUAS method and the MC limiter produce the most effective adaptive meshes. In Example 4.3, all methods behave similarly, although the SMUAS and BJK limiters resolve the layer slightly more sharply. For the Hemker problem (Example 4.4), the MUAS and BBK methods lead to well-distributed adaptive meshes, while the SMUAS method shows increased smearing. The BJK limiter, on the other hand, produces a less favorable adaptive grid, but still captures the layer sharply in the numerical solution.

Limiter	Accuracy	Approximation	Efficiency
BJK	++	+	○
MC	+	+	+
BBK	+	+	++
MUAS	+	+	++
SMUAS	○	+	○

Table 3: Summary of the numerical performance of the considered limiters.

Taken together, these results indicate that no single method is uniformly superior in approximation behaviour. The BJK limiter tends to produce the sharpest layers and therefore highly accurate solutions, whereas the MC, MUAS, and BBK methods interact more favorably with the residual-based estimator and therefore generate more effective adaptive meshes. Thus, the differences between the methods primarily reflect the interaction between stabilization and mesh refinement rather than a clear superiority of one method in approximation quality.

3. **Efficiency:** Efficiency is measured using both the number of nonlinear iterations and the overall computational time.

With respect to nonlinear iterations, the BJK limiter requires the largest number of iterations, whereas the MUAS, SMUAS, and BBK methods converge more rapidly. However, computational time tells a different story. The SMUAS method is significantly more expensive due to the gradient reconstruction used in the limiter, while the BBK method is the fastest. The MUAS method also performs efficiently and provides a good balance between iteration count and runtime.

Table 3 summarizes these observations. The symbols ++, +, and ○ indicate strong, moderate, and comparatively weaker performance, respectively. Overall, the results suggest that the BJK limiter is the most accurate method, the BBK and MUAS methods are the most efficient, and the MC limiter provides consistently good adaptive approximation.

The numerical study also reveals several open questions. In particular, the behaviour of the SMUAS limiter in the Hemker problem indicates that discrete maximum principle properties may depend not only on the mesh but also on the alignment of sharp layers with respect to the grid. Furthermore, the nonlinear example with solution-dependent convection demonstrates that limiter performance changes when the transport direction evolves during the nonlinear iteration. A theoretical understanding of algebraic stabilization schemes in such quasilinear settings, as well as the interaction between nonlinear stabilization and residual-based a posteriori estimators, remains an interesting topic for future research.

Acknowledgement. The authors would like to thank Prof. Dr. Volker John for discussions regarding the implementation of the SMUAS method. N.A. acknowledges support from the Gulf University for Science and Technology through grant ISG Case No. 96. A.J. acknowledges support from the Indian Institute of Technology Gandhinagar through grant IP/52016.

References

- [1] R. A. Adams. *Sobolev spaces*. Academic Press [A subsidiary of Harcourt Brace Jovanovich, Publishers], New York-London, 1975. Pure and Applied Mathematics, Vol. 65.
- [2] A. Allendes, G. R. Barrenechea, and R. Rankin. Fully computable error estimation of a nonlinear, positivity-preserving discretization of the convection-diffusion-reaction equation. *SIAM J. Sci. Comput.*, 39(5):A1903–A1927, 2017.

- [3] M. Augustin, A. Caiazzo, A. Fiebach, J. Fuhrmann, V. John, A. Linke, and R. Umla. An assessment of discretizations for convection-dominated convection–diffusion equations. *Computer Methods in Applied Mechanics and Engineering*, 200(47-48):3395–3409, November 2011.
- [4] I. Babuška and W. C. Rheinboldt. Error estimates for adaptive finite element computations. *SIAM J. Numer. Anal.*, 15(4):736–754, 1978.
- [5] G. R. Barrenechea, E. Burman, and F. Karakatsani. Edge-based nonlinear diffusion for finite element approximations of convection-diffusion equations and its relation to algebraic flux-correction schemes. *Numer. Math.*, 135(2):521–545, 2017.
- [6] G. R. Barrenechea, V. John, and P. Knobloch. Analysis of algebraic flux correction schemes. *SIAM Journal on Numerical Analysis*, 54(4):2427–2451, January 2016.
- [7] G. R. Barrenechea, V. John, and P. Knobloch. An algebraic flux correction scheme satisfying the discrete maximum principle and linearity preservation on general meshes. *Mathematical Models and Methods in Applied Sciences*, 27(03):525–548, March 2017.
- [8] G. R. Barrenechea, V. John, and P. Knobloch. Finite element methods respecting the discrete maximum principle for convection-diffusion equations. *SIAM Review*, 66(1):3–88, February 2024.
- [9] G. R. Barrenechea, V. John, and P. Knobloch. *Monotone discretizations for elliptic second order partial differential equations*, volume 61 of *Springer Series in Computational Mathematics*. Springer, Cham, [2025] ©2025.
- [10] G. R. Barrenechea, V. John, P. Knobloch, and R. Rankin. A unified analysis of algebraic flux correction schemes for convection-diffusion equations. *SeMA J.*, 75(4):655–685, 2018.
- [11] S. C. Brenner and L. R. Scott. *The mathematical theory of finite element methods*. Springer, New York, third edition, 2008.
- [12] A. N. Brooks and T. J. R. Hughes. Streamline upwind/Petrov-Galerkin formulations for convection dominated flows with particular emphasis on the incompressible Navier-Stokes equations. *Comput. Methods Appl. Mech. Engrg.*, 32(1-3):199–259, 1982. FENOMECH '81, Part I (Stuttgart, 1981).
- [13] T. A. Davis. Algorithm 832. *ACM Transactions on Mathematical Software*, 30(2):196–199, June 2004.
- [14] A. Demlow, S. Franz, and N. Kopteva. Maximum norm a posteriori error estimates for convection–diffusion problems. *IMA Journal of Numerical Analysis*, 43(5):2562–2584, February 2023.
- [15] W. Dörfler. A convergent adaptive algorithm for poisson’s equation. *SIAM Journal on Numerical Analysis*, 33(3):1106–1124, June 1996.
- [16] G. Hauke, M. H. Doweidar, and D. Fuster. A posteriori error estimation for computational fluid dynamics: the variational multiscale approach. In *Multiscale methods in computational mechanics*, volume 55 of *Lect. Notes Appl. Comput. Mech.*, pages 19–38. Springer, Dordrecht, 2011.
- [17] G. Hauke, M. H. Doweidar, D. Fuster, A. Gómez, and J. Sayas. Application of variational a-posteriori multiscale error estimation to higher-order elements. *Comput. Mech.*, 38(4-5):356–389, 2006.
- [18] G. Hauke, D. Fuster, and M. H. Doweidar. Variational multiscale a-posteriori error estimation for multi-dimensional transport problems. *Comput. Methods Appl. Mech. Engrg.*, 197(33-40):2701–2718, 2008.
- [19] P.W. Hemker. A singularly perturbed model problem for numerical computation. *Journal of Computational and Applied Mathematics*, 76(1-2):277–285, December 1996.

- [20] T. J. R. Hughes and A. Brooks. A multidimensional upwind scheme with no crosswind diffusion. In *Finite element methods for convection dominated flows (Papers, Winter Ann. Meeting Amer. Soc. Mech. Engrs., New York, 1979)*, volume 34 of *AMD*, pages 19–35. Amer. Soc. Mech. Engrs. (ASME), New York, 1979.
- [21] A. Jha. Hanging nodes for higher-order lagrange finite elements. *Examples and Counterexamples*, 1:100025, November 2021.
- [22] A. Jha. A residual based a posteriori error estimators for AFC schemes for convection-diffusion equations. *Computers & Mathematics with Applications*, 97:86–99, September 2021.
- [23] A. Jha. Residual-based a posteriori error estimators for algebraic stabilizations. *Appl. Math. Lett.*, 157:Paper No. 109192, 7, 2024.
- [24] A. Jha and V. John. A study of solvers for nonlinear AFC discretizations of convection–diffusion equations. *Computers & Mathematics with Applications*, 78(9):3117–3138, November 2019.
- [25] A. Jha and V. John. On basic iteration schemes for nonlinear AFC discretizations. In *Boundary and interior layers, computational and asymptotic methods—BAIL 2018*, volume 135 of *Lecture Notes in Computational Science and Engineering*, pages 113–128. Springer, Cham, 2020.
- [26] A. Jha, V. John, and P. Knobloch. Adaptive grids in the context of algebraic stabilizations for convection-diffusion-reaction equations. *SIAM Journal on Scientific Computing*, 45(4):B564–B589, August 2023.
- [27] A. Jha, Ondřej Pártl, Naveed Ahmed, and Dmitri Kuzmin. An assessment of solvers for algebraically stabilized discretizations of convection–diffusion–reaction equations. *Journal of Numerical Mathematics*, 31(2):79–103, April 2022.
- [28] V. John. A numerical study of a posteriori error estimators for convection-diffusion equations. *Comput. Methods Appl. Mech. Engrg.*, 190(5-7):757–781, 2000.
- [29] V. John and P. Knobloch. On spurious oscillations at layers diminishing (SOLD) methods for convection–diffusion equations: Part I – A review. *Computer Methods in Applied Mechanics and Engineering*, 196(17-20):2197–2215, March 2007.
- [30] V. John and P. Knobloch. On algebraically stabilized schemes for convection-diffusion-reaction problems. *Numerische Mathematik*, 152(3):553–585, 2022.
- [31] V. John, P. Knobloch, and O. Pártl. A numerical assessment of finite element discretizations for convection-diffusion-reaction equations satisfying discrete maximum principles. *Computational Methods in Applied Mathematics*, 2022.
- [32] V. John and J. Novo. A robust SUPG norm a posteriori error estimator for stationary convection–diffusion equations. *Computer Methods in Applied Mechanics and Engineering*, 255:289–305, March 2013.
- [33] P. Knobloch. *On the Application of Local Projection Methods to Convection–Diffusion–Reaction Problems*, page 183–194. Springer Berlin Heidelberg, 2009.
- [34] P. Knobloch. An algebraically stabilized method for convection–diffusion–reaction problems with optimal experimental convergence rates on general meshes. *Numerical Algorithms*, 94(2):547–580, April 2023.
- [35] P. Knobloch, D. Kuzmin, and A. Jha. Well-balanced convex limiting for finite element discretizations of steady convection-diffusion-reaction equations. *J. Comput. Phys.*, 518:Paper No. 113305, 18, 2024.

- [36] D. Kuzmin. On the design of general-purpose flux limiters for finite element schemes. I. Scalar convection. *J. Comput. Phys.*, 219(2):513–531, 2006.
- [37] D. Kuzmin. Algebraic flux correction for finite element discretizations of coupled systems. In M. Padračak, E. Oñate, and B. Schrefler, editors, *Proceedings of the Int. Conf. on Computational Methods for Coupled Problems in Science and Engineering*, pages 1–5. CIMNE, Barcelona, 2007.
- [38] D. Kuzmin. Monolithic convex limiting for continuous finite element discretizations of hyperbolic conservation laws. *Computer Methods in Applied Mechanics and Engineering*, 361:112804, 2020.
- [39] D. Kuzmin and J. Hämaläinen. *Finite element methods for computational fluid dynamics*, volume 14 of *Computational Science & Engineering*. Society for Industrial and Applied Mathematics (SIAM), Philadelphia, PA, 2015. A practical guide.
- [40] J. J. H. Miller, E. O’Riordan, and G. I. Shishkin. *Fitted Numerical Methods For Singular Perturbation Problems: Error Estimates in the Maximum Norm for Linear Problems in One and Two Dimensions*. WORLD SCIENTIFIC, February 2012.
- [41] H.-G. Roos, M. Stynes, and L. Tobiska. *Robust numerical methods for singularly perturbed differential equations. Convection-diffusion-reaction and flow problems*. Springer-Verlag, Berlin, second edition, 2008.
- [42] L. Tobiska and R. Verfürth. Robust a posteriori error estimates for stabilized finite element methods. *IMA J. Numer. Anal.*, 35(4):1652–1671, 2015.
- [43] R. Verfürth. Robust a posteriori error estimates for nonstationary convection-diffusion equations. *SIAM J. Numer. Anal.*, 43(4):1783–1802, 2005.
- [44] R. Verfürth. *A posteriori error estimation techniques for finite element methods*. Numerical Mathematics and Scientific Computation. Oxford University Press, Oxford, 2013.
- [45] U. Wilbrandt, C. Bartsch, N. Ahmed, N. Alia, F. Anker, L. Blank, A. Caiazzo, S. Ganesan, S. Giere, G. Matthies, R. Meesala, A. Shamim, J. Venkatesan, and V. John. ParMooN—a modernized program package based on mapped finite elements. *Computers & Mathematics with Applications*, 74(1):74–88, July 2017.
- [46] S. T. Zalesak. Fully multidimensional flux-corrected transport algorithms for fluids. *J. Comput. Phys.*, 31(3):335–362, 1979.
- [47] Z. Zhao, H. Li, and W. Gao. The numerical study of a continuous Petrov-Galerkin method for the nonlinear convection-diffusion equation. *J. Math. Anal. Appl.*, 550(2):Paper No. 129617, 20, 2025.